Composite Structures 142 (2016) 254–262

Contents lists available at ScienceDirect

Composite Structures

journal homepage: www.elsevier.com/locate/compstruct

Experimental response of additively manufactured metallic pentamode materials confined between stiffening plates

A. Amendola [a], C.J. Smith [b], R. Goodall [b], F. Auricchio [c], L. Feo [a], G. Benzoni [d], F. Fraternali [a,*]

[a] Department of Civil Engineering, University of Salerno, Via Giovanni Paolo II 132, 84084 Fisciano (SA), Italy
[b] Department of Materials Science and Engineering, University of Sheffield, Mappin Street, Sheffield S1 3JD, UK
[c] Department of Civil Engineering and Architecture, University of Pavia, Via Ferrata 3, 27100 Pavia, Italy
[d] Department of Structural Engineering, University of California at San Diego, La Jolla, CA 92093-0411, USA

ARTICLE INFO

Article history:
Available online 28 January 2016

Keywords:
Pentamode lattices
Additive manufacturing
Effective elastic moduli
Inelastic response

ABSTRACT

An experimental investigation on the mechanical response of confined pentamode lattices in the elastic and post-yield regimes is presented. An Electron Beam Melting facility is employed to additively manufacture pentamode lattices confined by terminal plates in a titanium alloy. The given experimental results show that the geometry of the microstructure, and the macroscopic aspect ratio of the confined lattices strongly influence the lateral and vertical stiffness properties of the structure. The post-elastic response of the analyzed materials features acceptable energy dissipation capacity. The presented results highlight several analogies between the mechanical response of confined pentamode lattices and that of elastomeric bearings formed by soft rubber pads and stiffening steel or fiber-reinforced composite layers. They pave the way to future studies on the use of pentamode materials for the fabrication of innovative seismic isolation devices and/or shear-wave band gap systems.

1. Introduction

Extremal materials that are receiving increasing interest are the so-called pentamode lattices, which consist of diamond-like lattices featuring five soft modes of deformation (unit cell with four rods meeting at a point) [1]. Such lattices exhibit very low shear moduli (theoretically equal to zero) [1], and may be able to stop or dramatically attenuate shear waves [2]. Physical models of pentamode materials have been fabricated through additive manufacturing (AM) techniques over the last few years, both at the macro- [3] and at the micro-scale [4]. Schittny et al. [3] have studied the experimental behavior of macroscopic, polymeric samples of pentamode lattices in the elastic regime: the results obtained by such authors prove that the elastic moduli of pentamode materials are strongly related to the geometry of the lattice micro-structure, being markedly affected by the dimensions of the rods forming the lattice, and particularly sensitive to the ratio between the diameter d of the connections between the rods and the lattice constant a. The experimental Young's modulus E of the lattice has been found approximately three times stiffer than the experimental shear modulus G. The results presented in [3] also show that the ratio between the bulk modulus B and the shear modulus G strongly increases by reducing the contact area between the rods. Similar results have been found at the micro-scale by Kadic et al. [4]. Polymeric samples of pentamode lattices have been fabricated by such authors using dip-in direct-laser-writing (DLW) optical lithography, a technique well suited to build three-dimensional structures across a range of scales from micro to small [5]. Experimental and numerical results given in [3,4] demonstrate that the mechanical behavior of pentamode lattices replicates that of fluids in the limit of $d \to 0$, when the shear modulus G tends to zero. For finite, nonzero values of d, it has been found that the B/G ratio is extremely high, even if G is positive and nonzero [3,4]. Because of their unusual mechanical features, pentamode materials have been proposed for transformation acoustics and elasto-mechanical cloak (refer, e.g., to the recent paper [6] and the references therein), but their potential in different engineering fields is still only partially explored.

The present study investigates the elastic and post-elastic responses of additively manufactured pentamode lattices confined between stiffening plates. We analyze metallic samples obtained through additive manufacturing by Electron Beam Melting (EBM) of a powder of the titanium alloy Ti–6Al–4V [7,8,10], for different aspect ratios of the unit-cell, and two macroscale aspect ratios

* Corresponding author.
E-mail addresses: adaamendola1@unisa.it (A. Amendola), chrisjsmith@sheffield.ac.uk (C.J. Smith), r.goodall@sheffield.ac.uk (R. Goodall), auricchio@unipv.it (F. Auricchio), l.feo@unisa.it (L. Feo), gbenzoni@ucsd.edu (G. Benzoni), f.fraternali@unisa.it (F. Fraternali).

http://dx.doi.org/10.1016/j.compstruct.2016.01.091
0263-8223/

(slender and thick samples). We find that the confinement of pentamode lattices between stiffening plates greatly affects the elastic response of the overall structure, compared with the case of unconfined, infinite pentamode lattices [11]. The obtained results highlight several similarities between the elastic response of confined pentamode materials and the analogous response of elastomeric bearings composed of rigid steel or fiber-reinforced composite layers and soft layers of natural or synthetic rubber [12–18]. Concerning the post-elastic response, we observe that the examined pentamode materials feature acceptable energy dissipation capacity, and ranges of supplemental damping in line with values of common isolation devices. The remainder of the paper is structured as follows. We begin in Section 2.1 by illustrating the EBM-manufactured pentamode materials analyzed in the present study. Next, we provide a description of the in-house experimental setup employed to subject such materials to lateral and vertical force–displacement tests (Section 2.2). Section 3 presents the results of laboratory tests aimed at determining the elastic moduli (Section 3.1) and the post-elastic energy dissipation properties (Section 3.2) of the analyzed materials. Concluding remarks and directions for future research are presented in Section 4.

2. Materials and methods

2.1. Physical models of confined pentamode materials

We manufactured pentamode lattices confined by stiffening plates and made by the titanium alloy Ti–6Al–4V (hereafter simply denoted by Ti6Al4V) through the Arcam S12 EBM facility at the Department of Materials Science and Engineering, University of Sheffield. Such an additive manufacturing (AM) technology allows the manufacture of features with size down to 0.4 mm by progressively depositing, heating and melting layers of Ti6Al4V powder, with the melted regions in each layer defined according to a CAD model of the specimen to be manufactured [7,8]. It is worth noting that the size of the specimen designed by CAD does not correspond perfectly to the built object. The beam scan strategies and the surface roughness can result in larger (in diameter) printed members [10]. The main properties of the employed titanium alloy, when in the fully dense state, are given in Table 1 [19]. The EBM process has also been shown to fabricate lattice structures with certain members that are undersized [20]. But here it was also shown that this affect can be completely alleviated for thin members if the use of perimeter melting (known as contouring) is excluded. Therefore all of the pentamode lattice specimens were fabricated using a back-and-forth raster melt pattern only (known as hatching).

Fig. 1 shows the extended face-centered-cubic (fcc) unit cell of a pentamode lattice formed by sixteen rods that are composed of two truncated bi-cones featuring large diameter D at the mid-span and small diameter d at the extremities [2–6]. Upon selecting the lattice constant $a = 30$ mm and $D = 2.72$ mm ($D/a \approx 9\%$), we manufactured pentamode specimens with the unit cell shown in Fig. 1, using three different values of d: $d_1 = 0.49$ mm ($d_1/a = 1.6\%$); $d_2 = 1.04$ mm ($d_2/a = 3.5\%$); and $d_3 = 1.43$ mm ($d_3/a = 4.8\%$, cf. Table 2). It is worth remarking that the limit $d/a \to 0$ corresponds to a perfectly pin-jointed lattice (stretching-dominated response), while the case with $d/a > 0$ corresponds to a lattice featuring nonzero bending rigidities of nodal junctions and rods, which deforms through both stretching of rods and bending of rods and nodes [11].

Table 1
Main physical and mechanical properties of the fully dense isotropic polycrystalline Ti6Al4V titanium alloy [19].

Mass density [g/cm^3]	4.42
Yield strength [MPa]	910.00
Young's modulus [GPa]	120.00
Poisson's ratio	0.342

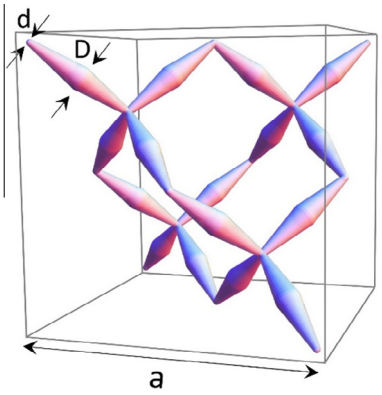

Fig. 1. Extended fcc unit cell of the pentamode lattices analyzed in the present study.

Table 2
Geometrical parameters of the EBM built pentamode materials (CAD sizes in brackets).

	a [mm]	D [mm]	d_1 [mm]	d_2 [mm]	d_3 [mm]
Built size (CAD size)	30 (30)	2.72 (2.71)	0.49 (0.45)	1.04 (0.90)	1.43 (1.35)

We additively manufactured two different sets of pentamode specimens:

(a) "*Slender pentamode materials*" (SPM): obtained by replicating the extended fcc unit cell of Fig. 1 2×2 times in the horizontal plane, 4 times along the vertical axis, and confining the $2 \times 2 \times 4$ lattice between Ti6Al4V plates with 80 mm edge and $t_p = 1$ mm thickness (see Fig. 2);
(b) "*Thick pentamode materials*" (TPM): obtained by replicating the extended fcc unit cell of Fig. 1 2×2 times in the horizontal plane, 2 times along the vertical axis, and confining the $2 \times 2 \times 2$ lattice between the above mentioned plates (see Fig. 3).

Hereafter, we name SPM1, SPM2 and SPM3 the SPM-specimens with $d = d_1$, $d = d_2$, and $d = d_3$, respectively. Similarly, we name TPM1, TPM2 and TPM3 the TPM-specimens with $d = d_1$, $d = d_2$, and $d = d_3$, respectively. We built three different SPM specimens and one TPM specimen for each analyzed d/a ratio.

It is well known that the EBM manufacturing process creates solid material with some level of porosity (typically below 0.2% if suitable parameters for the alloy are used in the machine) instead of fully dense materials for both solid structures [9] and those intended to contain free space [8]. Based on a recent, detailed study of porosity in EBM titanium made with the same conditions used for the current material [9], we hereafter assume the internal porosity of such a material is of the order of 0.2%, and its Young modulus E_m is therefore approximately equal to that of the fully dense Ti6Al4V alloy (Table 1).

2.2. Experimental setup

An in-house experimental setup was assembled to apply lateral force–displacement histories under constant vertical load on the pentamode specimens described in the previous section (Fig. 4).

An L-shaped plate, sliding vertically over linear bearings, allows the application of the vertical load through calibrated weights. The

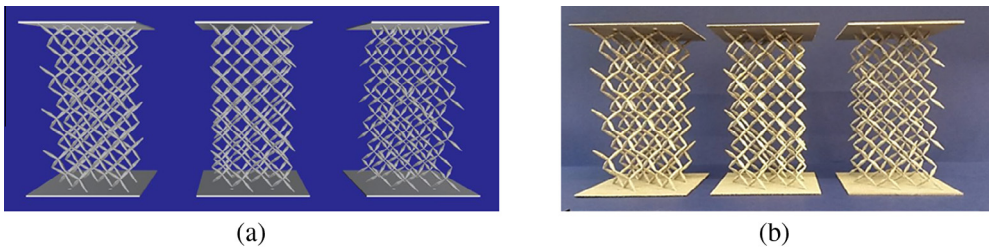

Fig. 2. CAD (a) and EBM (b) models of slender (SPM) specimens ($2 \times 2 \times 4$ extended unit cells).

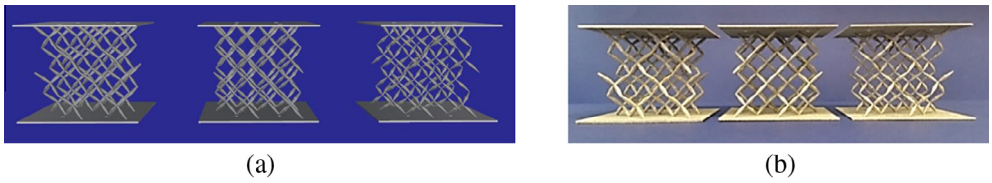

Fig. 3. CAD (a) and EBM (b) models of thick (TPM) specimens ($2 \times 2 \times 2$ extended unit cells).

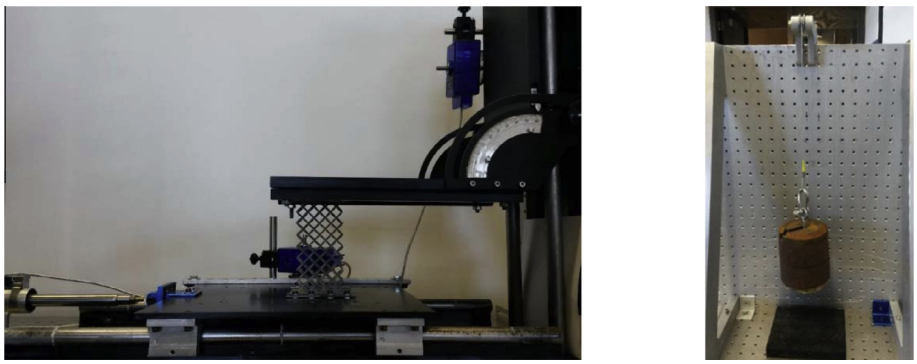

Fig. 4. Left: overall view of the experimental setup. Right: counter balancing system introduced to remove platen self-weight.

selfweight of the plate is removed with a counter balancing system of pulley and weights (Fig. 4). The top base of the specimen is firmly connected to the plate by clamping strips located all around the base edges. The same clamping mechanism is applied to the bottom base of the specimen that is connected to the horizontally sliding table (Fig. 5). Horizontal displacements are applied through an actuator connected to the sliding table and reacting against a solid metal block. The force rating of the actuator is 300 lb (1.3 kN), with a displacement range of ±100 mm. Forces are acquired by a load cell installed between the back of the actuator and the reaction block. Vertical and lateral displacements are measured with rotary motion sensors.

The same setup allows the application of the vertical load through calibrated weights while no horizontal motion is applied.

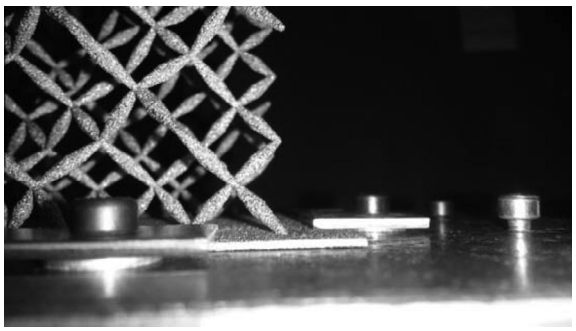

Fig. 5. Connection of the specimen to the sliding table.

With this procedure compression tests were completed by manual application of weights and automatic recording of vertical displacements of the plate. Preliminary to any actual test, the setup was subjected to a shakedown phase to assess the frictional force components and to verify alignments and parallelisms. The test data were consistently processed with the removal of friction from the testing equipment.

3. Experimental results

The present section illustrates the results of the laboratory tests that we conducted to characterize the mechanical response of the pentamode materials illustrated in Section 2.1. We begin by estimating the elastic moduli of slender and thick pentamode materials through cyclic lateral force–displacement tests at constant vertical loading, and monotonic vertical force–displacement tests under zero horizontal force (Section 3.1). Next, we investigate the inelastic response of the analyzed materials via (cyclic and monotonic) lateral force–displacement tests conducted up to specimen's failure (Section 3.2). Fig. 6 illustrates pictures of selected slender and thick specimens extracted from in-situ videos of lateral force–displacement tests.

3.1. Estimation of the elastic moduli

The estimation of the elastic moduli of slender and thick specimens was conducted through cyclic lateral force (F_h) vs. lateral displacement (δ_h) tests in displacement control at the displacement rate $\dot{\delta}_h = 0.8$ mm/s (hereafter also referred to as "*shear*

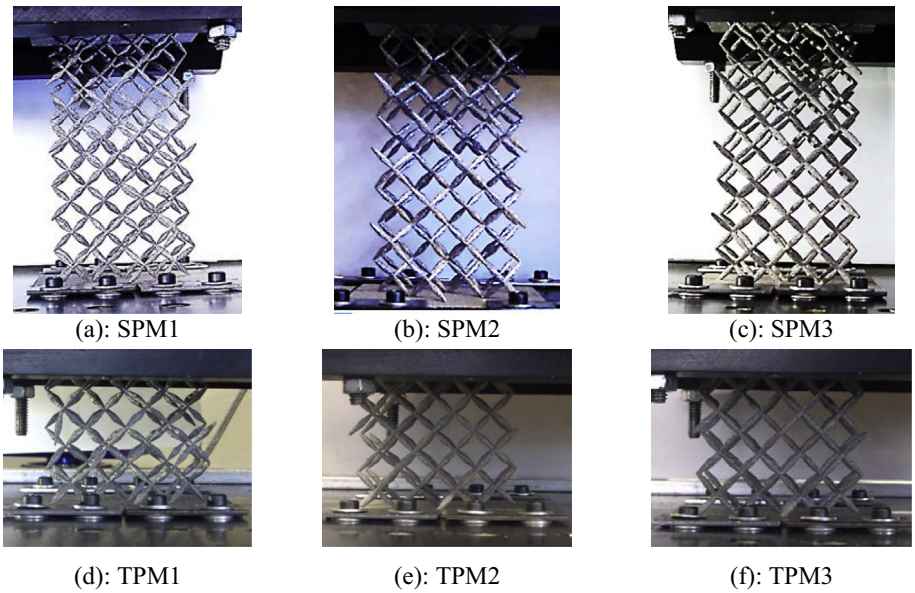

Fig. 6. Frames from in-situ videos of lateral displacement tests on SPM and TPM specimens.

tests"). Such a study considered three different (constant) values of the applied vertical load: $F_v = 22.67$ N, $F_v = 45.34$ N, and $F_v = 68.00$ N, and one specimen for each examined d/a ratio (cf. Fig. 7–10; Tables 3–5). The analyzed values of the vertical load were accurately chosen so that to not cause permanent deformation of the specimens. We also conducted cyclic $F_h - \delta_h$ tests at the strain rates of 0.8 mm/s and 2.4 mm/s on the specimen SPM3 (Table 4), and vertical force (F_v) vs. vertical displacement (δ_v) compression tests on SPM and TPM specimens, on considering one specimen for each examined d/a ratio ("*compression tests*", cf. Tables 3 and 5).

3.1.1. Slender specimens

Fig. 7 illustrates the results of cyclic tests conducted on slender specimens for constant $F_v = 45.34$ N, and lateral displacements $\delta_h \approx \pm 3$ mm (three cycles for each specimen at $\dot{\delta}_h = 0.8$ mm/s). The results in Fig. 7 highlight an albeit limited hysteretic response of the SPM specimens in the examined range of lateral displacements (especially in the case of the SPM3 specimen). Such a phenomenon is explained by internal stress intensification effects

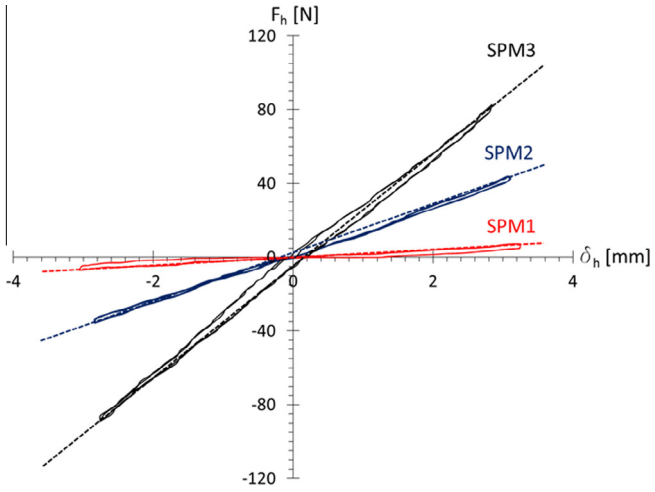

Fig. 7. Lateral force–displacement curves under constant vertical load ($F_v = 45.34$ N) for slender specimens (dashed lines: effective secant responses).

Table 3
Solid volume fraction ϕ and experimental values of the effective horizontal stiffness $K_{h,eff}$; effective shear modulus G_{eff}; effective vertical stiffness $K_{v,eff}$; and effective compression modulus E_{eff} of SPM specimens.

		SPM1	SPM2	SPM3
$\phi \times 10^3$		8.14	11.75	15.04
$K_{h,eff}$ (N/mm)	Mean	2.10	13.23	31.38
	(Std dev)	(0.159)	(0.237)	(0.598)
G_{eff} (kPa)		70.43	444.77	1054.69
$K_{v,eff}$ (N/mm)	Mean	14.92	100.69	242.95
	(Std dev)	(0.278)	(≈ 0)	(≈ 0)
E_{eff} (kPa)		501.49	3384.47	8165.70

Table 4
Experimental values of $K_{h,eff}$ for specimen SPM3 under different strain rates ($F_v = 45.34$ N).

	$\dot{\delta}_h = 0.8$ mm/s	$\dot{\delta}_h = 2.4$ mm/s
$K_{h,eff}$ (N/mm)	30.73	29.95

Table 5
Solid volume fraction ϕ and experimental values of the effective horizontal stiffness $K_{h,eff}$; effective shear modulus G_{eff}; effective vertical stiffness $K_{v,eff}$; and effective compression modulus E_{eff} of TPM specimens.

		TPM1	TPM2	TPM3
$\phi \times 10^3$		8.14	11.75	15.04
$K_{h,eff}$ (N/mm)	Mean	13.10	62.67	115.54
	(Std dev)	(0.117)	(0.270)	(0.662)
G_{eff} (kPa)		222.04	1061.90	1957.77
$K_{v,eff}$ (N/mm)	Mean	38.83	175.37	503.89
	(Std dev)	(0.605)	(0.602)	(0.001)
E_{eff} (kPa)		657.98	2971.50	8538.12

causing pseudo-elastic response, due to micro-plasticity events, before macro-yielding [23]. This effect would be increased in lattice samples as the structure results in areas of stress concentration being present in the sample, with the potential for the stress to reach high levels locally, while the specimen is macroscopically not highly loaded. Comparing the results in Fig. 7 and the

envelopes of cyclic and monotonic tests provided in Section 3.2 (cf. Fig. 11 and Table 6), we note lateral displacements in the range $|\delta_h| \leqslant 3$ mm reached in Fig. 7 are below the deflection points of the $F_h-\delta_h$ curves in Fig. 11. Hereafter, we refer to such points where there is large scale departure from linearity in the force–displacement behavior as "macro-yield" points [23]. Very similar results were obtained for $F_v = 22.67$ N and $F_v = 68.02$ N. We refer to the line connecting the extreme points of the cyclic lateral force displacements curves as the "*effective*" secant response of the specimen [12]. Similarly, we let $K_{h,eff}$ denote the effective (secant) stiffness defined as follows

$$K_{h,eff} = \frac{|F_h^+| + |F_h^-|}{|\delta_l^+| + |\delta_l^-|} \tag{1}$$

where the symbols + and – denote the maximum and minimum value, respectively.

Table 3 shows the mean values ("Mean") and standard deviations ("Std dev") of the experimental values of the secant stiffness $K_{h,eff}$, which were obtained for the SPM specimens under the analyzed values of the vertical load F_v, and the strain rate $\dot{\delta}_h = 0.8$ mm/s. The same table also shows the values of the effective shear modulus defined as follows

$$G_{eff} = \overline{K}_{h,eff} \cdot \frac{h}{A} \tag{2}$$

where $\overline{K}_{h,eff}$ denotes the mean value of $K_{h,eff}$; $h = 4a + t_p$ denotes the total height of the specimen (including the heights of the pentamode lattice and the terminal bases); and $A = 2a \times 2a$ denotes the lattice covered area of the terminal plates. The results in Fig. 7 and Table 3 highlight a marked increase of $K_{h,eff}$ with increasing values of the "microstructure" aspect ratio d/a. Such a phenomenon can be ascribed to the higher bending stiffness of the lattice with larger nodal junctions [11]. A small dispersion of $K_{h,eff}$ with the vertical load F_v is observed in the displacement regime $|\delta_h| \leqslant 3$ mm.

Table 3 includes data extracted from compression tests, which refers to the effective vertical stiffness $K_{v,eff}$ defined as follows

$$K_{v,eff} = \frac{F_v^{\max}}{\delta_v^{\max}} \tag{3}$$

where $F_v^{\max}$ denotes the maximum applied vertical load, and $\delta_v^{\max}$ denotes the corresponding vertical displacement. Table 3 shows statistics of the experimental values of the vertical secant stiffness $K_{v,eff}$ obtained for each SPM specimen through three different measurements, and the values of the effective compression modulus defined as follows

$$E_{eff} = \overline{K}_{v,eff} \cdot \frac{h}{A} \tag{4}$$

where $\overline{K}_{v,eff}$ denotes the mean value of $K_{v,eff}$. By examining the results of shear and compression tests for current specimens, we find that the E_{eff}/G_{eff} ratio is equal to 7.12 in SPM1, 7.61 in SPM2 and 7.90 in SPM3. It is worth observing that such a ratio is approximately equal to one for (unconfined) many-cells pentamode lattices, according to the theory of elastic networks presented in Ref. [11]. It is also interesting comparing our current findings with the numerical and experimental results presented by Schittny et al. in [3] for 3D printed pentamode lattices in polymeric materials with the same macroscopic aspect ratio ($2 \times 2 \times 4$ extended unit cells). Such lattices feature $a = 15$ mm, and exhibit similar microscopic aspect ratios, as compared to the current specimen, i.e., $D/a \approx 9\%$, and d/a varying between 1.5% and 9.0%. Schittny et al. experimentally observe the following ratios between the Young modulus E and the shear modulus G: $E/G \approx 3.67$ for lattices with $d/a = 1.6\%$ (lattices with microscopic aspect ratios similar to SPM1 specimens); $E/G \approx 5.52$ for $d/a = 3.5\%$ (similar to SPM2), and $E/G \approx 5.21$ for $d/a = 4.8\%$ (similar to SPM3). Numerical results obtained by such authors through 3D finite element simulations [3,4] instead predict E/G ratios ranging between 4.29 and 4.97 for the same lattices. The significant increase of the E_{eff}/G_{eff} ratio of SPM specimens over the E/G ratio predicted by the theory presented in [11] is explained by the stiffening effect played by the terminal bases that confine such specimens. For what concerns the increase of E_{eff}/G_{eff} over the E/G ratios given in [3], it is worth noting that the current metallic specimens feature larger and stiffer bases, as compared to the polymeric specimens studied Schittny et al. in [3].

We now pass to study the dependence of the effective moduli G_{eff} and E_{eff} on the solid volume fraction ϕ of the lattice (defined as the volume of rods per unit volume of material). We construct linear and quadratic fitting models of the experimental data presented in Table 3, via the NonlinearModelFit function of *Mathematica*® 10 (models of the form $k_1\phi$ and $k_2\phi^2$, respectively). The results in Fig. 8 show that quadratic models better fit the scaling laws of G_{eff}/E_m and E_{eff}/E_m with ϕ, featuring remarkably lower Root Mean Square Errors (RMSE) than linear models. Such an observation leads us to conclude that SPM specimens exhibit bending-dominated response under the examined tests [21,22].

Let us now investigate the influence of strain rate effects on the shear response of a SPM3 specimen, by comparing experimental values of $K_{h,eff}$ under cyclic shear tests featuring $\dot{\delta}_h = 0.8$ mm/s and $\dot{\delta}_h = 2.4$ mm/s. The results in Table 4 show that such values of $K_{h,eff}$ differ each other only by 2.6%, which suggests that the examined strain rates play a limited role of on the elastic lateral response of the current specimen.

3.1.2. Thick specimens

Fig. 9 shows the results of cyclic lateral force–displacement tests performed on thick specimens at $\dot{\delta}_h = 0.8$ mm/s, for $F_v = 45.34$ N (cf. also Table 5, which includes mean values and standard deviations of $K_{h,eff}$ for $F_v = 22.67$ N, $F_v = 45.34$ N, and $F_v = 68.02$ N).

The results in Fig. 9 confirm the presence of the micro-scale hysteresis before macro-yielding already observed in slender

Table 6
Coordinates and ductility values of noticeable points of the curves in Fig. 11.

		F_a [N]	δ_a [mm]	μ_a	F_b [N]	δ_b [mm]	μ_b	F_c [N]	δ_c [mm]	μ_c
SPM1	Monotonic	15.92	5.85	1.00	32.93	26.74	4.57	16.20	32.67	5.58
	Cyclic	12.70	5.02	1.00	20.19	10.29	2.06	17.67	12.35	2.47
SPM2	Monotonic	152.38	10.98	1.00	206.83	22.97	2.09	100.01	35.03	3.19
	Cyclic	143.10	10.23	1.00	195.12	15.75	1.54	157.03	21.26	2.07
SPM3	Monotonic	485.01	15.79	1.00	545.56	29.92	1.89	268.5	40.64	2.57
	Cyclic	480.12	15.70	1.00	514.00	21.70	1.38	280.00	28.65	1.82
TPM1	Cyclic	25.22	2.00	1.00	40.20	4.17	2.08	40.20	4.17	2.08
TPM2	Cyclic	262.18	4.11	1.00	407.34	8.53	2.07	357.45	9.76	2.37
TPM3	Cyclic	467.93	4.55	1.00	899.02	16.88	2.70	899.02	16.88	2.70

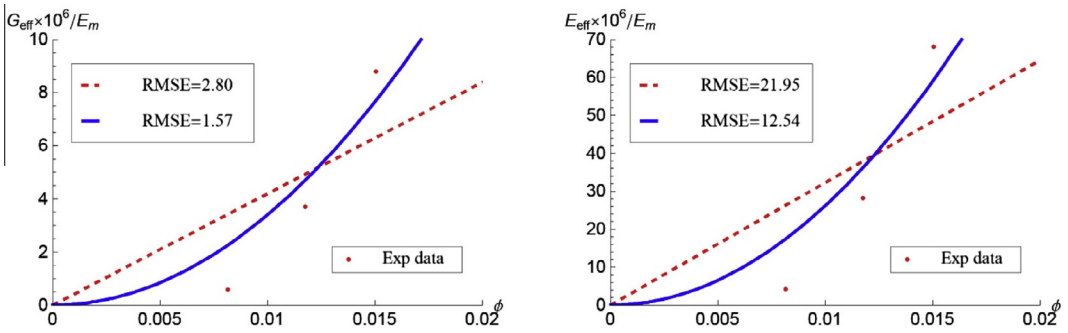

Fig. 8. Linear and quadratic fitting models of the scaling laws of G_{eff}/E_m and E_{eff}/E_m with the solid volume fraction ϕ for SPM specimens.

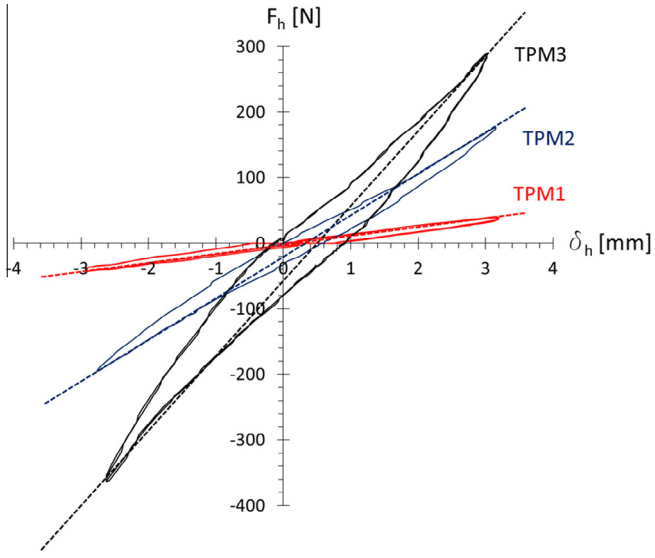

Fig. 9. Lateral force–displacement curves under constant vertical load ($F_v = 45.34$ N) for thick specimens (dashed lines: effective secant responses).

specimens. Such a phenomenon is more pronounced in TPM specimens than slender specimens, especially in presence of large-size nodal junctions (TPM2 and TPM3). From the plots in Fig. 8 and the results in Table 5 we observe marked increases of $K_{h,eff}$ with increasing d/a ratios (i.e., when passing from TPM1 to TPM3), and small dispersions of such a quantity with the examined values of the vertical load F_v, as in the case of slender specimens. Estimates of the effective vertical stiffness $K_{v,eff}$ and the effective compression modulus E_{eff} for TPM specimens were obtained through vertical force–displacement tests performed as in the case of slender specimens (cf. Table 5).

The E_{eff}/G_{eff} ratio for thick specimens is equal to 2.96 in TPM1, 2.80 in TPM2 and 4.36 in TPM3. For what concerns the scaling laws of G_{eff} and E_{eff} with ϕ, the results in Fig. 10 show that quadratic models better fit experimental data of TPM specimens than linear models, as we already observed in Section 3.1.1 (bending-dominated response [21,22]).

3.2. Post-elastic response

We investigated the post-elastic response of SPM and TPM specimens by conducting cyclic lateral force–displacement tests in displacement control up to specimen's failure (under the vertical load $F_v = 44.45$ N, and the strain rate $\dot{\delta}_h = 0.8$ mm/s, cf. Figs. 11 and 12). In the case of SPM specimens, we also performed monotonic lateral force–displacement tests up to specimen's failure (Fig. 11). All such tests were carried out starting from the virgin state, for a single specimen of each microstructure aspect ratio d/a (cf. Section 2.1). Fig. 11 shows the measured envelope force–displacement F_h–δ_h curves, where the labels a, b and c indicate the final point of the initial linear branch, the peak of horizontal force and the failure point, respectively. For these specimens, point c corresponds to the ultimate vertical bearing capacity. The actual F_h–δ_h curves of the monotonic tests on SPM specimens showed marked oscillations in the unstable phase characterized by a decrease of F_h for increasing values of δ_h, due to progressive joint failure. The final collapse of the specimen occurred due to the rupture of several terminal nodes placed along the stretched diagonals (Fig. 13). The results in Fig. 11 highlight an initial hardening branch of the post-elastic response of each examined specimen. Such a branch is followed by a second post-elastic branch with negative tangent stiffness, which progressively leads the specimen to collapse. The coordinates of the above *a*–*b*–*c* points are provided in Table 6, together with the ductility values computed as follows

$$\mu = \frac{\delta_h - \delta_{h,el}}{\delta_{h,el}} \tag{5}$$

where δ_h is the current value of the lateral displacement, and $\delta_{h,el}$ is the lateral displacement in correspondence to point *a*.

The cyclic tests in Fig. 12 where performed at controlled ductility on a SPM1 and a TPM3 specimen, by letting the maximum lateral displacement to grow progressively in such a way that it results $\mu = 0.25$ in the first cycle; μ grows with step 0.25 in the next cycles up to $\mu = 1.00$; and, finally, μ grows with step 0.50 in the post-elastic cycles up to specimen's failure. Fig. 11-left shows a comparison between the measured envelopes of cyclic tests and monotonic tests on SPM specimens, which highlights the fact that the envelopes of the monotonic tests always lie above those of the cyclic tests in the post-elastic range, due to (low-cycle) fatigue-damage [24].

Post-yield stiffness degradation is a common observation in a range of different tests and lattice designs of EBM manufactured Ti6Al4V porous structures (e.g., [8,10]), due to progressive brittle fracture of individual struts of the lattice from the point of first macroscopic yield [7].

Table 7 shows the Energy Dissipated per Cycle *EDC*; the effective viscous damping ξ_{eff}; the post-yield (K_d) vs. elastic (K_e) stiffness ratio $|K_d - K_e|/K_e$; and characteristic strength Q_d, defined as force at zero horizontal displacement (cf. point 8.2.1.2.2 of [25]), for the SPM1 and TPM3 specimens analyzed in Fig. 12.

The effective damping in Table 7 is defined in line with the European standard on anti-seismic devices EN 15129:2009 [25], and corresponds to the energy dissipated E_{diss} through the following formula

$$\xi_{eff} = \frac{E_{diss}}{2\pi K_{h,eff}\,\delta^2_{h,\max}} \tag{6}$$

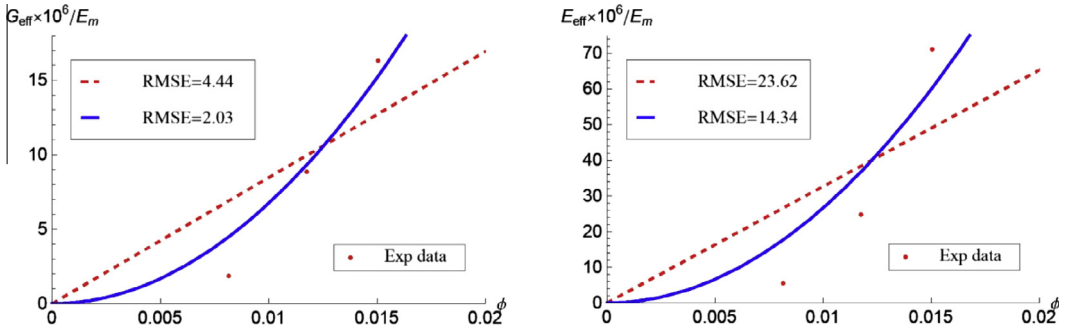

Fig. 10. Linear and quadratic fitting models of the scaling laws of G_{eff}/E_m and E_{eff}/E_m with the solid volume fraction ϕ for TPM specimens.

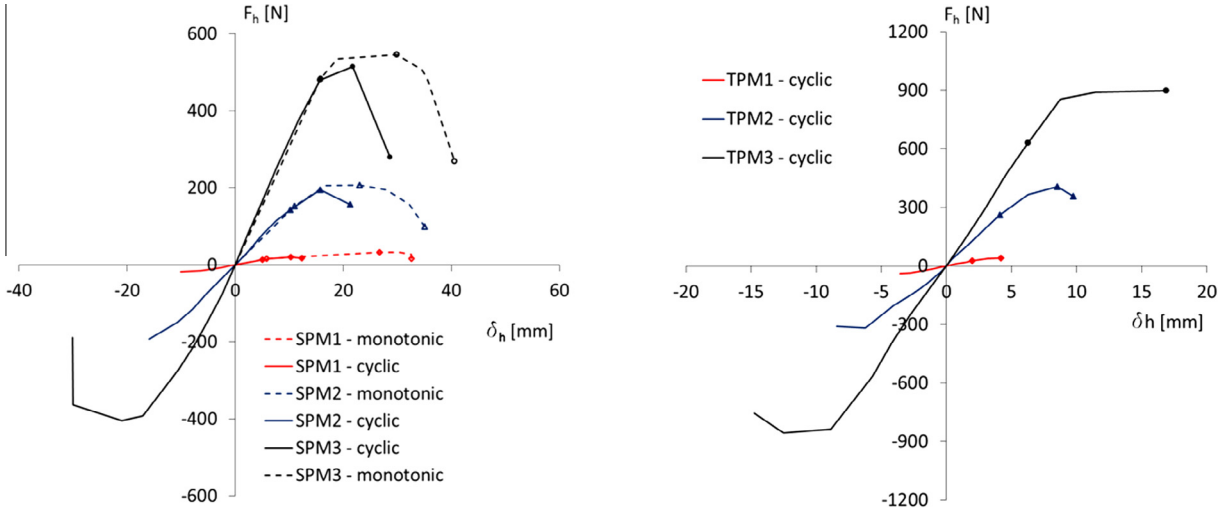

Fig. 11. Measured envelops of cyclic (solid lines) and monotonic (dashed lines) lateral force–displacement tests.

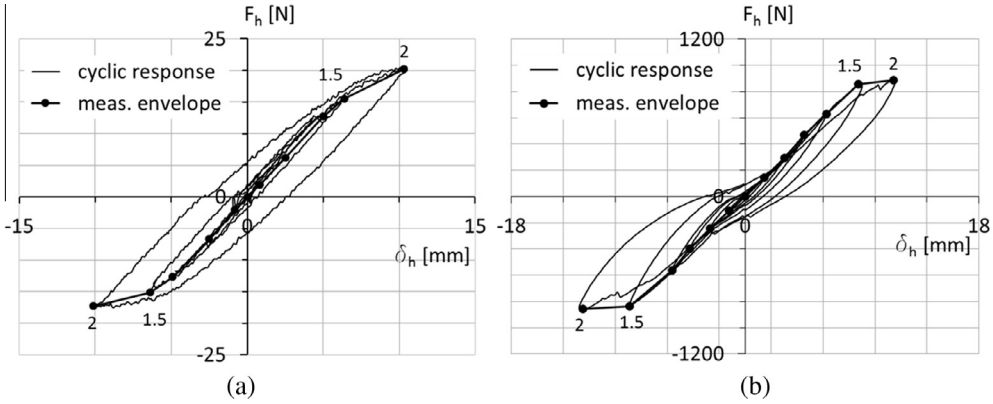

Fig. 12. Lateral force–displacement responses of a SPM1 (a) and a TPM3 (b) specimen under cyclic tests at constant vertical load $F_v = 45.34$ N (solid curves: measured envelope curves; numbers indicate ductility).

Table 7
Energy dissipation per cycle (E_{diss}); effective viscous damping (ξ_{eff}); post-yield vs. elastic stiffness ratio ($|K_d - K_e|/K_e$); and characteristic strength (Q_d) at different post-elastic cycles of lateral force–displacement test on SPM1 and TPM3 specimens.

		EDC (10^3 kN·mm)	ξ_{eff} (%)	$\lvert K_d - K_e\rvert/K_e$ (%)	Q_d (N)
SPM1	$\mu_{max} = 1.5$	191.44	25.11	25.73	1.52
	$\mu_{max} = 2.0$	406.27	31.12	57.44	5.27
TPM3	$\mu_{max} = 1.5$	$12.97\cdot10^3$	28.02	10.07	93.12
	$\mu_{max} = 2.0$	$18.86\cdot10^3$	30.12	88.73	95.01

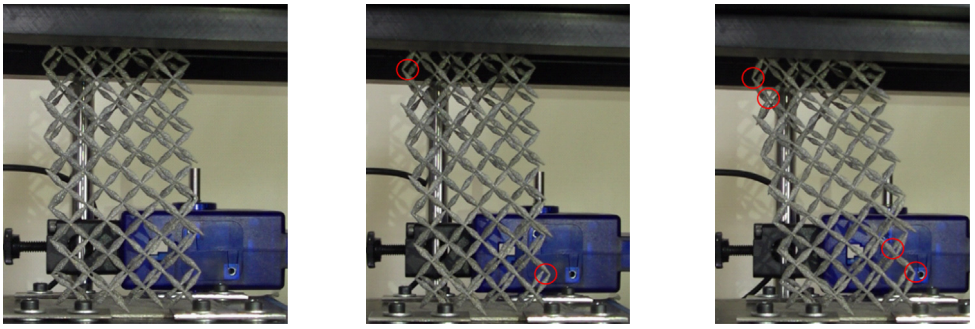

(a) SPM1 – 3^{rd} *elastic cycle* $\delta_h = 5.12$ mm, $\mu = 1.0$

(b) SPM1 - 1^{st} *inelastic cycle* $\delta_h = 6.40$ mm, $\mu = 1.5$

(c) SPM1 - 2^{nd} *inelastic cycle* $\delta_h = 10.29$, $\mu = 2.0$

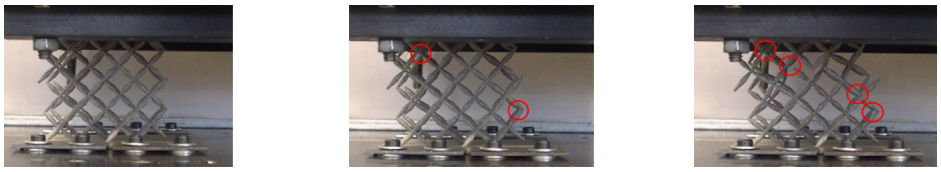

(d) TPM3 - 4^{th} *elastic cycle* $\delta_h = 6.25$ mm, $\mu = 1.0$

(e) TPM3 - 1^{st} *inelastic cycle* $\delta_h = 8.74$ mm, $\mu = 1.5$

(f) TPM3 - 2^{nd} *inelastic cycle* $\delta_h = 11.45$ mm, $\mu = 2.0$

Fig. 13. Frames from in-situ videos of lateral displacement tests on a SPM1 (a–c) and a TPM3 (d–f) specimen. The circled struts are affected by fracture damage.

where $K_{h,eff}$ is the effective secant stiffness, and $\delta_{h,\max}$ is the maximum lateral displacement of the current cycle (see point 3.1.10 of [25]). The results in Table 7 highlight progressive increases of ξ_{eff}, $|K_d - K_e|/K_e$, and Q_d with the amplitude of the maximum lateral displacement (i.e., with $\mu_{\max}$), due to progressive fracture of lattice struts [8] (cf. Fig. 13). The results in terms of energy dissipated per cycle (and effective damping) while indicating a progressive increase with displacement show also values of supplemental damping (25–30%) that are suitable for seismic isolation applications. The failure mechanisms in Fig. 13 indicate a quite symmetric pattern of broken elements between top and bottom of the specimen. It was also observed that during the tests the failure of struts happened in a rather smooth progression and in expected locations. This performance new configurations that can significantly increase the required structural ductility to be forseen.

4. Concluding remarks

We have experimentally investigated the response of EBM printed Ti6Al4V specimens of pentamode materials confined between stiffening plates, under lateral and vertical force–displacement tests. The examined tests were aimed at researching the effective shear and compression properties of such systems, and their inelastic response under cyclic and monotonic loading histories. We have examined a collection of specimens that differ in microstructural and macrostructural aspect ratios, which are related to the size of the nodal junctions (microstructure aspect ratio) and the ratio between the number of unit cells placed in the vertical and horizontal directions (macrostructure aspect ratio).

Several results of the present study highlight analogies between the mechanical response of the analyzed systems and that of elastomeric bearings consisting of alternating layers of synthetic or natural rubber and stiffening layers made of steel plates or fiber-reinforced composites, which are commonly used as bridge support devices or seismic or vibration isolators for buildings [12–18]. We have observed that the ratio between the effective compression modulus E_{eff} and the effective shear modulus G_{eff} of the analyzed pentamode materials is markedly affected by the presence of the stiffening plates, as compared to available theoretical predictions of the E/G ratio of unconfined pentamode lattices [11]. Such a stiffening effect is larger in the case of slender specimens and large-size nodal junctions, since the E_{eff}/G_{eff} ratio varies between 7.93, in case of the SPM3 specimen, and 2.96, in case of the TPM1 specimen (cf. Section 3.1). It replicates the stiffening role played by steel layers in elastomeric bearings. It is worth noting, however, that the absolute vertical and lateral stiffness coefficients of the examined pentamode materials increase when passing from slender to thick specimens (cf. Section 3.1).

Despite the very preliminary nature of this study on feasibility for base isolation applications, some observations support the potential of pentamode structures for use in anti-seismic system development and/or as shear-wave band gap systems [2]. The strict dependency of the response by the geometry of the lattice allows the design of structures of controlled performance. The ranges of supplemental damping observed for the specimens are well in line with values of common isolation devices. The levels of energy dissipated is acceptable and could be significantly improved by reducing material porosity, using different construction techniques, materials, and/or through the insertion of dissipative lead-cores within the pentamode isolator [12,15]. Additional horizontal ductility and vertical stiffness is expected to be developed also using different configurations that will provide more confinement to the single layers of the pentamode structure.

We address the design and modeling of highly dissipative pentamode bearings and impact mitigation devices to future work, on employing either manual assembling procedures [26], layered structures showing different materials and/or lattice geometries in different layers, and additive manufacturing techniques in polymeric and metallic materials [3,4,7].

Acknowledgments

Support for this work was received from the Italian Ministry of Foreign Affairs, Grant no. PGR00173/2015, Italy-USA Scientific and Technological Cooperation 2015.

References

[1] Milton GW, Cherkaev AV. Which elasticity tensors are realizable? J Eng Mater-Technol 1995;117(4):483–93.
[2] Martin A, Kadic M, Schittny R, Bückmann T, Wegener M. Phonon band structures of three-dimensional pentamode metamaterials. Phys Rev B 2010;86:155116.
[3] Schittny M, Bückmann T, Kadic M, Wegener M. Elastic measurements on macroscopic three-dimensional pentamode metamaterials. Appl Phys Lett 2013;103:231905.
[4] Kadic M, Bückmann T, Stenger N, Thiel M, Wegener M. On the practicability of pentamode mechanical metamaterials. Appl Phys Lett 2012;100:191901.
[5] Buckmann T, Stenger N, Kadic M, Kaschke J, Frölich A, Kennerknecht T, et al. Tailored 3D mechanical metamaterials made by dip-in direct-laser-writing optical lithography. Adv Mater 2012;24(20):2710–4.
[6] Bückmann T, Thiel M, Kadic M, Schittny R, Wegener M. An elastomechanical unfeelability cloak made of pentamode metamaterials. Nat Commun 2014;5:4130.
[7] Amendola A, Nava EH, Goodall R, Todd I, Skelton RE, Fraternali F. On the additive manufacturing and testing of tensegrity structures. Compos Struct 2015;131:66–71.
[8] Hernandez-Nava E, Smith CJ, Derguti F, Tammas-Williams S, Leonard F, Withers PJ, et al. The effect of density and feature size on mechanical properties of isostructural metallic foams produced by additive manufacturing. Acta Mater 2015;85:387–95.
[9] Tammas-Williams S, Zhao H, Léonard F, Derguti F, Todd I, Prangnell PB. XCT analysis of the influence of melt strategies on defect population in Ti–6Al–4V components manufactured by selective electron beam melting. Mater Charact 2015;102:47–61.
[10] van Grunsven W, Hernandez-Nava E, Reilly GC, Goodall R. Fabrication and mechanical characterisation of titanium lattices with graded porosity. Metals 2014;4(3):401–9.
[11] Norris AN. Mechanics of elastic networks. Proc R Soc London A 2014;470(522):1–18.
[12] Constantinou MC, Whittaker AS, Kalpakidis Y, Fenz DM, Warn GP. Performance of seismic isolation hardware under service and seismic loading, Technical Report MCEER-07-0012; 2007.
[13] Skinner RI, Robinson WH, McVerry GH. An introduction to seismic isolation. Wiley; 1993.
[14] Kelly JM. Earthquake-resistant design with rubber. London: Springer-Verlag; 1993.
[15] Benzoni G, Casarotti C. Effects of vertical load, strain rate and cycling on the response of lead-rubber seismic isolators. J Earthquake Eng 2009;13(3):293–312.
[16] Toopchi-Nezhad H, Tait MJ, Drysdale RG. Bonded versus unbonded strip fiber reinforced elastomeric isolators: finite element analysis. Compos Struct 2014;93(2):850–9.
[17] Osgooei PM, Tait MJ, Konstantinidis D. Three-dimensional finite element analysis of circular fiber-reinforced elastomeric bearings under compression. Compos Struct 2014;108(1):191–204.
[18] Osgooei PM, Tait MJ, Konstantinidis D. Finite element analysis of unbonded square fiber-reinforced elastomeric isolators (FREIs) under lateral loading in different directions. Compos Struct 2014;113(1):164–73.
[19] Metals Handbook, (2) Properties and selection: nonferrous alloys and special-purpose materials. Metals Park, OH: ASM International; 1990
[20] Smith CJ, Derguti F, Hernandez Nava E, Thomas M, Tammas-Williams S, Gulizia S, Fraser D, Tood I. Dimensional accuracy of Electron Beam Melting (EBM) additive manufacture with regard to weight optimized truss structures. J Mater Process Tech 2016;229:128–38.
[21] Meza LR, Das S, Greer JR. Strong, light weight, and recoverable three-dimensional ceramic nanolattices. Science 2014;6202(345):1322–6.
[22] Schaedler TA, Jacobsen AJ, Torrents A, Sorensen AE, Lian J, Greer JR, et al. Ultralight metallic microlattices. Science 2011;6058(334):962–5.
[23] Steele RK, McEvily AJ. The high-cycle fatigue behavior of Ti–6Al–4V alloy. Eng Fract Mech 1976;8:31–7.
[24] Szachogluchowicz I, Sniezek L, Hutsaylyuk V. Low cycle fatigue properties laminate AA2519–TI6AL4V. Procedia Eng 2015;114:26–33.
[25] European Committee for Standardization. Anti-seismic devices, EN 15129. Brussels: Belgium; 2009.
[26] Amendola A, Carpentieri G, de Oliveira M, Skelton RE, Fraternali F. Experimental investigation of the softening stiffening response of tensegrity prisms under compressive loading. Compos Struct 2014;117:234–43.